



From Sub-Rayleigh to Supershear Ruptures During Stick-Slip Experiments on Crustal Rocks

François X. Passelègue *et al.*

Science **340**, 1208 (2013);

DOI: 10.1126/science.1235637

This copy is for your personal, non-commercial use only.

If you wish to distribute this article to others, you can order high-quality copies for your colleagues, clients, or customers by [clicking here](#).

Permission to republish or repurpose articles or portions of articles can be obtained by following the guidelines [here](#).

The following resources related to this article are available online at www.sciencemag.org (this information is current as of June 6, 2013):

Updated information and services, including high-resolution figures, can be found in the online version of this article at:

<http://www.sciencemag.org/content/340/6137/1208.full.html>

Supporting Online Material can be found at:

<http://www.sciencemag.org/content/suppl/2013/06/05/340.6137.1208.DC1.html>

This article **cites 29 articles**, 9 of which can be accessed free:

<http://www.sciencemag.org/content/340/6137/1208.full.html#ref-list-1>

This article appears in the following **subject collections**:

Geochemistry, Geophysics

http://www.sciencemag.org/cgi/collection/geochem_phys

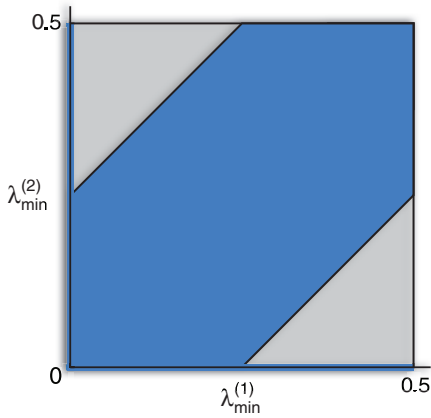


Fig. 3. Witnessing genuine multipartite entanglement. The figure displays the 2D cross section through the six-qubit eigenvalue polytope where we fix $\lambda_{\min}^{(3)} = \dots = \lambda_{\min}^{(6)} = 0.125$. If the local eigenvalues do not belong to any of the biseparable entanglement polytopes (blue region), then all corresponding pure states necessarily contain genuine six-qubit entanglement.

the global state to estimate the purity (22). Whereas it is an experimental challenge to achieve the levels of purity necessary for the application of our method, we believe that they are in the reach of current technology (23–25).

References and Notes

1. G. Vidal, *Phys. Rev. Lett.* **91**, 147902 (2003).
2. D. Leibfried *et al.*, *Science* **304**, 1476 (2004).
3. V. Giovannetti, S. Lloyd, L. Maccone, *Science* **306**, 1330 (2004).
4. R. Horodecki, P. Horodecki, M. Horodecki, K. Horodecki, *Rev. Mod. Phys.* **81**, 865 (2009).
5. C. H. Bennett, S. Popescu, D. Rohrlich, J. A. Smolin, A. V. Thapliyal, *Phys. Rev. A* **63**, 012307 (2000).
6. W. Dür, G. Vidal, J. I. Cirac, *Phys. Rev. A* **62**, 062314 (2000).
7. D. M. Greenberger, M. A. Horne, A. Zeilinger, in *Bell's Theorem, Quantum Theory, and Conceptions of the Universe*, M. Kafatos, Ed. (Kluwer, 1989), pp. 69–72.
8. F. Verstraete, J. Dehaene, B. De Moor, H. Verschelde, *Phys. Rev. A* **65**, 052112 (2002).
9. M. Christandl, G. Mitchison, *Commun. Math. Phys.* **261**, 789 (2006).
10. A. Klyachko, Quantum marginal problem and representations of the symmetric group, arXiv:quant-ph/0409113 (2004).
11. S. Daftuar, P. Hayden, *Ann. Phys.* **315**, 80 (2005).
12. A. J. Coleman, V. I. Yukalov, *Reduced Density Matrices: Coulson's Challenge* (Springer, 2000).
13. A. Klyachko, *J. Phys. Conf. Ser.* **36**, 72 (2006).
14. Further details can be found in the supplementary text on Science Online.
15. M. Brion, in *Séminaire d'Algèbre P. Dubreil et M.-P. Malliavin*, M. P. Malliavin, Ed. (Springer, 1987), pp. 177–192.
16. H. Derksen, G. Kemper, *Computational Invariant Theory* (Springer, 2002).
17. B. Doran, F. Kirwan, *Pure Appl. Math. Q.* **3**, 61 (2007).
18. Y.-J. Han, Y.-S. Zhang, G.-C. Guo, *Phys. Rev. A* **70**, 042309 (2004).

19. O. Gühne, G. Toth, H. J. Briegel, *New J. Phys.* **7**, 229 (2005).
20. R. E. Borland, K. Dennis, *J. Phys. B* **5**, 7 (1972).
21. K. Furuya, M. C. Nemes, G. Q. Pellegrino, *Phys. Rev. Lett.* **80**, 5524 (1998).
22. H. Buhrman, R. Cleve, J. Watrous, R. de Wolf, *Phys. Rev. Lett.* **87**, 167902 (2001).
23. A. Rauschenbeutel *et al.*, *Science* **288**, 2024 (2000).
24. J.-W. Pan, M. Daniell, S. Gasparoni, G. Weihs, A. Zeilinger, *Phys. Rev. Lett.* **86**, 4435 (2001).
25. T. Monz *et al.*, *Phys. Rev. Lett.* **106**, 130506 (2011).
26. M. Walter, B. Doran, D. Gross, M. Christandl, www.entanglement-polytopes.org (2012).

Acknowledgments: We thank A. Botero, F. Brandão, P. Bürgisser, C. Ikenmeyer, F. Kirwan, F. Mintert, G. Mitchison, A. Osterloh, and P. Vrana for valuable discussions. This work is supported by the German Science Foundation (grant CH 843/2-1), the Swiss National Science Foundation [grants PP00P2_128455, 20CH21_138799 (CHIST-ERA project CQC), and 200021_138071], the Swiss National Center of Competence in Research Quantum Science and Technology, and the Excellence Initiative of the German Federal and State Governments (grant ZUK 43). After completion of this work, we have learned about independent related work by Sawicki, Ozmanic, and Kuš.

Supplementary Materials

www.sciencemag.org/cgi/content/full/340/6137/1205/DC1
 Supplementary Text
 Figs. S1 to S4
 Tables S1 to S3
 References (27–82)
 19 November 2012; accepted 25 April 2013
 10.1126/science.1232957

From Sub-Rayleigh to Supershear Ruptures During Stick-Slip Experiments on Crustal Rocks

François X. Passelègue,^{1*} Alexandre Schubnel,¹ Stefan Nielsen,² Harsha S. Bhat,³ Raúl Madariaga¹

Supershear earthquake ruptures propagate faster than the shear wave velocity. Although there is evidence that this occurs in nature, it has not been experimentally demonstrated with the use of crustal rocks. We performed stick-slip experiments with Westerly granite under controlled upper-crustal stress conditions. Supershear ruptures systematically occur when the normal stress exceeds 43 megapascals (MPa) with resulting stress drops on the order of 3 to 25 MPa, comparable to the stress drops inferred by seismology for crustal earthquakes. In our experiments, the sub-Rayleigh-to-supershear transition length is a few centimeters at most, suggesting that the rupture of asperities along a fault may propagate locally at supershear velocities. In turn, these sudden accelerations and decelerations could play an important role in the generation of high-frequency radiation and the overall rupture-energy budget.

Earthquake damage depends, in part, on the velocity of the rupture front (*I*). In 1973, Burridge demonstrated theoretically that in-plane shear ruptures (mode II) could propagate

at velocities higher than the shear wave velocity (*C_s*) and up to the compressional wave velocity (*C_p*) (2). Since then, so-called supershear ruptures (*V_r* > *C_s*, where *V_r* is rupture velocity) have been observed during large strike-slip earthquakes (3–8). The stress and geometric conditions leading to the transition between sub-Rayleigh and supershear ruptures have been investigated with photoelasticity, both theoretically (9, 10) and experimentally, on brittle polymers (11–15). Although these experiments successfully illus-

trate supershear ruptures, the lack of experiments on rock samples limits the ability to understand these rare events observed in nature. In a recent experimental study, a photoelastic setup was coupled with an acoustic high-frequency-recording multistation array during stick-slip experiments on polycarbonate sheets. This allowed Schubnel *et al.* to use high-frequency acoustics to identify unequivocally the signature of both sub-Rayleigh and supershear ruptures (15). This advance has opened the possibility of revisiting experimental work performed on rocks (16–19).

Here, we report results from stick-slip experiments conducted on saw-cut Westerly granite samples (fig. S1), which serve as proxies for crustal rocks, during triaxial loading (where the

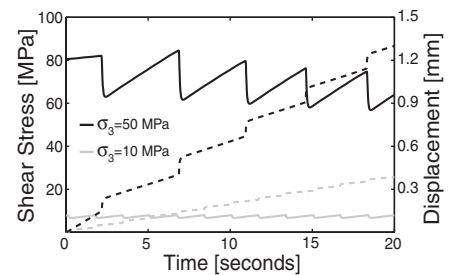


Fig. 1. Stress release during microearthquakes. Evolution of shear stress (solid lines) and displacement (dashed lines) is represented for two stick-slip experiments conducted at 10- and 50-MPa confining pressure.

¹Laboratoire de Géologie, CNRS UMR 8538, École Normale Supérieure, 75005 Paris, France. ²Istituto Nazionale di Geofisica e Vulcanologia, Roma 00143, Italy. ³Institut de Physique du Globe de Paris, 1 rue Jussieu, 75238 cedex 05 Paris, France.

*Corresponding author. E-mail: passelegue@geologie.ens.fr

principal stresses $\sigma_1 > \sigma_2 = \sigma_3$). Stick-slip experiments and earthquake mechanisms are analogous in nature because they both result from rapid frictional sliding along preexisting faults, leading to partial or total stress drop (16). In our experiments, the stress conditions were typical of the upper crust, ranging from 10 to 150 MPa in normal stress acting on the preexisting fault. In total, we recorded more than 200 stick-slip events (Fig. 1). For each event, we inverted the rupture velocity directly from our experimental records, using high-frequency acoustics as a tracking tool (fig. S2).

We used recorded accelerograms to track the Mach wavefront arrival. Theoretical arrival time of the Mach wavefront radiated away from the rupture tip was predicted using (i) the position of the rupture front determined from the inverted rupture velocity (fig. S2) and (ii) the shear wave

velocity and the distance between the Mach front antenna (MFA) sensors to the fault, as defined in Fig. 2A (15). Our calculation assumes that the rupture velocity is constant. Importantly, we looked for ruptures with V_r greater than the shear wave speed but different than $\sqrt{2}C_s$, for in this case, no Mach cone is expected (20).

We compared our calculation with waveforms recorded by the MFA array for a stick-slip event during which a supershear rupture velocity was predicted by the inversion (Fig. 2B). In agreement with theory (21), we first observed a weak P -wave arrival, which corresponds to the continuous emission of P waves by the rupture tip as it propagates. However, the signal is dominated by the arrival of a large-amplitude, coherent wavefront just after the diffuse P -wave arrival. The relative amplitude of this wavefront, when compared to the first P -wave amplitude,

increases with distance to the fault. This is expected because the geometric attenuation of a conic wavefront is smaller than that of spherical one. At each station, the arrival time of this wavefront is consistent with the predicted arrival time of the Mach wavefront.

To confirm our estimations of the rupture velocity, we used two-dimensional (2D) steady-state rupture model to conduct simulations (21). We observe an excellent fit, both in relative amplitude and for the general waveform shape, when comparing the experimental waveforms recorded on the MFA sensors during a subshear event and the synthetics obtained by our numerical simulation (Fig. 3B). We observed similar good correspondence between experimental waveforms and simulation of a supershear rupture (Fig. 3C). In both cases, we obtained the best fit between analytical and experimental records by using the rupture velocity estimated experimentally, confirming that our experimental estimate of the rupture velocity is accurate. Furthermore, we show that dynamic rupture models that can accurately simulate strong ground motions on the kilometeric scale can also simulate accelerations in the kilohertz range on centimetric sized samples. In other words, dynamic rupture propagation is truly a self-similar mechanism.

Our experimental results demonstrate that the ruptures were dominantly mode II (fig. S3). For this mode, the transition between sub-Rayleigh and supershear rupture has been extensively discussed in theoretical and experimental studies (9, 12–15). Following 2D numerical studies, this transition is generally explained in terms of the seismic ratio $S = (\tau_p - \tau_o)/(\tau_o - \tau_r)$ where τ_p , τ_o , and τ_r are the peak frictional strength, the initial shear stress, and the residual frictional strength, respectively. The ratio τ_o/σ_n (where σ_n is the normal stress), employed by Ben-David *et al.* (14), is equivalent to S , and both quantities are simply related by $\tau_o/\sigma_n = (f_s - f_d)/(1 + S) + f_d$ (where f_s and f_d are the static and dynamic friction coefficients, respectively) (Fig. 4). In our experiments, τ_o was continuously measured (Fig. 1). Taking $f_s = 0.85$ and $f_d = 0.1$, S could be estimated for each individual stick-slip. Supershear propagation may happen under both of the following conditions: (i) $S < S_c$ (where S_c , the critical value of S allowing supershear transition, is equal to 1.77 or 1.119 in 2D and 3D, respectively), which was always the case in our experiments (Fig. 4A), and (ii) when the rupture length exceeds the transition length L , estimated following the semi-empirical relation (9)

$$L = \frac{39.2}{\pi(1-\nu)} \frac{1}{(S_c - S)^3} \frac{\mu G}{\left[\sigma_n \left(\frac{f_s - f_d}{1 + S}\right)\right]^2} \quad (1)$$

where ν , μ , and G are, respectively, the Poisson ratio, the shear modulus, and the fracture energy. In our case, condition (ii) can be met only if $L < L_f$, where L_f is the finite length of the experimental fault. In our experiments, G may range from

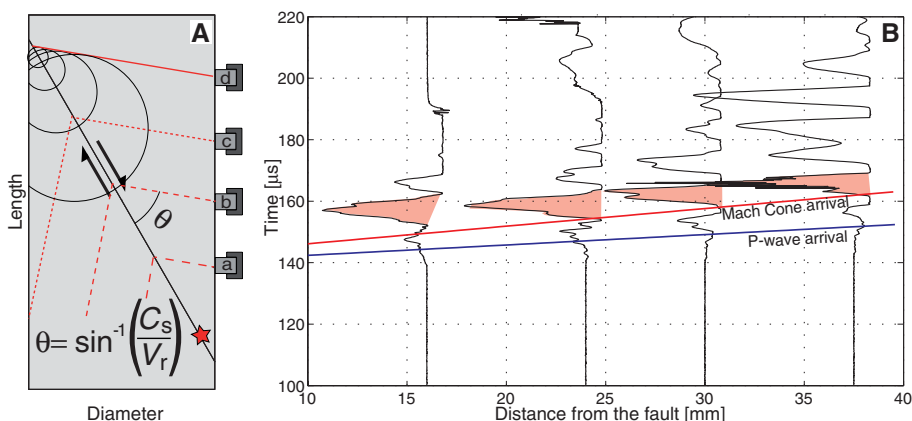


Fig. 2. Mach wavefront arrival. (A) Schematic of the Mach cone arrival at MFA stations. The red star represents the nucleation zone of the event. Arrows indicate the sense of shear (here, right lateral). The positions of the MFA stations a to d are shown relative to the fault plane. θ , is the angle of the Mach cone, a function of the ratio between the rupture and shear wave velocities. (B) Waveforms recorded on the MFA array during a supershear event that occurred at $\tau = 84$ and $\sigma_n = 99$ MPa. Blue and red solid lines represent the first P -wave front and the S -wave Mach front, respectively. The Mach front is shaded in red.

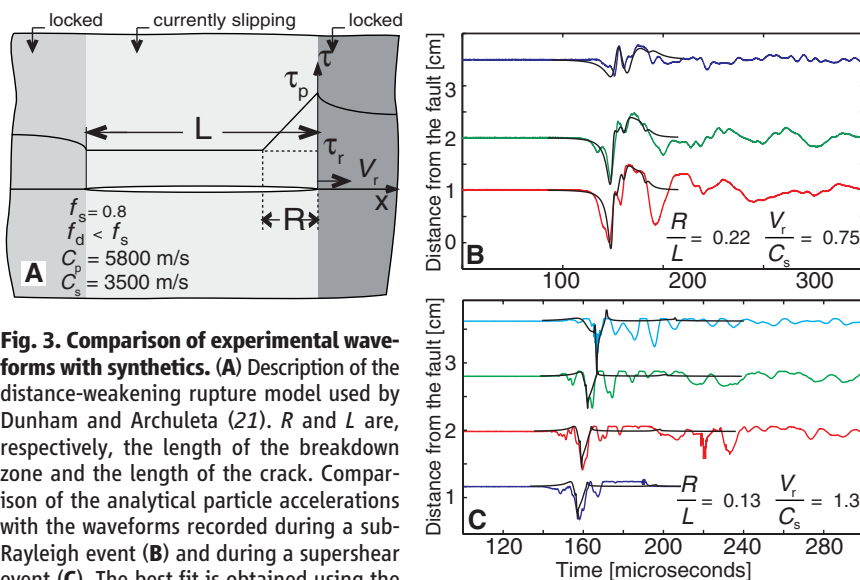


Fig. 3. Comparison of experimental waveforms with synthetics. (A) Description of the distance-weakening rupture model used by Dunham and Archuleta (21). R and L are, respectively, the length of the breakdown zone and the length of the crack. Comparison of the analytical particle accelerations with the waveforms recorded during a sub-Rayleigh event (B) and during a supershear event (C). The best fit is obtained using the inverted rupture velocity.

the lower bound 10 J/m^2 , as given by single-crystal fracture energy values and stick-slip experiments performed at low normal stress (19), to the upper bound 10^4 J/m^2 , measured for intact Westerly granite samples at high confining pressures (22). From Eq. 1, L was calculated as a function of normal stress in two cases: (i) $S = 1$ and $G = 10 \text{ J/m}^2$ and (ii) $S = 0$ and $G = 1000 \text{ J/m}^2$ (Fig. 4A). Experiments performed at the lowest normal stresses are compatible with $G \approx 10 \text{ J/m}^2$. However, experiments performed at intermediate normal stresses can be explained only by using larger fracture energy. This is consistent with our observation of an intense production of fine gouge particles at intermediate and high normal stresses. Indeed, for spherical particles, the ratio between G and surface energy of single crystals (γ) is $G/\gamma \approx 3w/d$, where w is the fault thickness and d is the average particle size. Our observation of gouge particles of $1\text{-}\mu\text{m}$ diameter and smaller is consistent with a fault roughness of less than $30 \mu\text{m}$. The match between the measured rupture velocities and the prediction that the minimum transition length L drops to a few centimeters (comparable to

our sample size) at high normal stress (Fig. 4A) explains why, in our experiments, supershear rupture becomes a “normal” phenomena for $\sigma_n > 60 \text{ MPa}$. It also explains why supershear ruptures were not clearly observed in previous experimental studies on rocks conducted at low normal stress (most often in biaxial conditions) (18, 19).

Finally, we observe a double correlation between the rupture velocity, the initial stress ratio τ_0/σ_n , and the final stress drop (Fig. 4B). Subshear ruptures occurred for stress ratios $\tau_0/\sigma_n < 0.6$ and resulted in stress drops generally lower than 1.5 MPa . Conversely, supershear ruptures occurred for stress ratios $\tau_0/\sigma_n > 0.7$ and resulted in stress drops generally larger than 3 MPa . These results not only make sense physically but are also compatible with values previously observed on brittle polymers (14) and with field observations for the Kunlunshan earthquake (23). Importantly, our findings are comparable to the average stress drops inferred by seismologists for most large crustal earthquakes. Note that our direct measurement of the stress drop is comparable to what a seismological estimate would be using the final slip u (fig. S4).

Based on our experimental results, why is there a paucity of supershear ruptures observed in nature? A first straightforward explanation is related to the difference in fault geometry between our experiments and seismogenic faults. Our experiments consisted of a perfectly planar fault geometry with very low initial roughness at high normal stress, leading to uniform and large stresses on the fault plane. Seismogenic faults, on the other hand, are most often nonplanar and exhibit self-affine roughness (24). The occurrence of kinks and dilatational jogs could slow down or even arrest locally the propagation of seismic ruptures (25). The few documented examples of supershear earthquakes are on very smooth, planar fault sections (3–8). In addition, the presence of a gouge layer along the fault interface may slow the propagation of the rupture, as well as thermo-hydro-mechanical coseismic processes within the breakdown zone [such as thermal pressurization (26), frictional melting (27), mineral reactions (28), and off fault damage, including pulverization (29)], which dissipate part of the released strain energy available, resulting in a deceleration of the rupture front. Alternatively, the paucity of supershear rupture observation in nature might also be due to limitations in instrumentation and/or spatial coverage. Nevertheless, the experimental values of L and stress drops reported here for a classical crustal lithology (Westerly granite) under upper-crustal conditions ($<150 \text{ MPa}$) demonstrate that rupture velocity may exhibit important variations at the scale of small (centimetric) asperities, so that the seismological estimate of rupture velocities over long fault segments is an average that could well have little importance at the scale of an asperity. Our experimental results strongly suggest that, despite the scarcity of compelling measurements on natural earthquakes, supershear ruptures may frequently occur at the local scale of asperities, for which the stress drop generally inferred is quite large. In turn, these sudden accelerations and decelerations of the rupture front should play an important role in generating high-frequency radiation, which will influence the total rupture-energy budget.

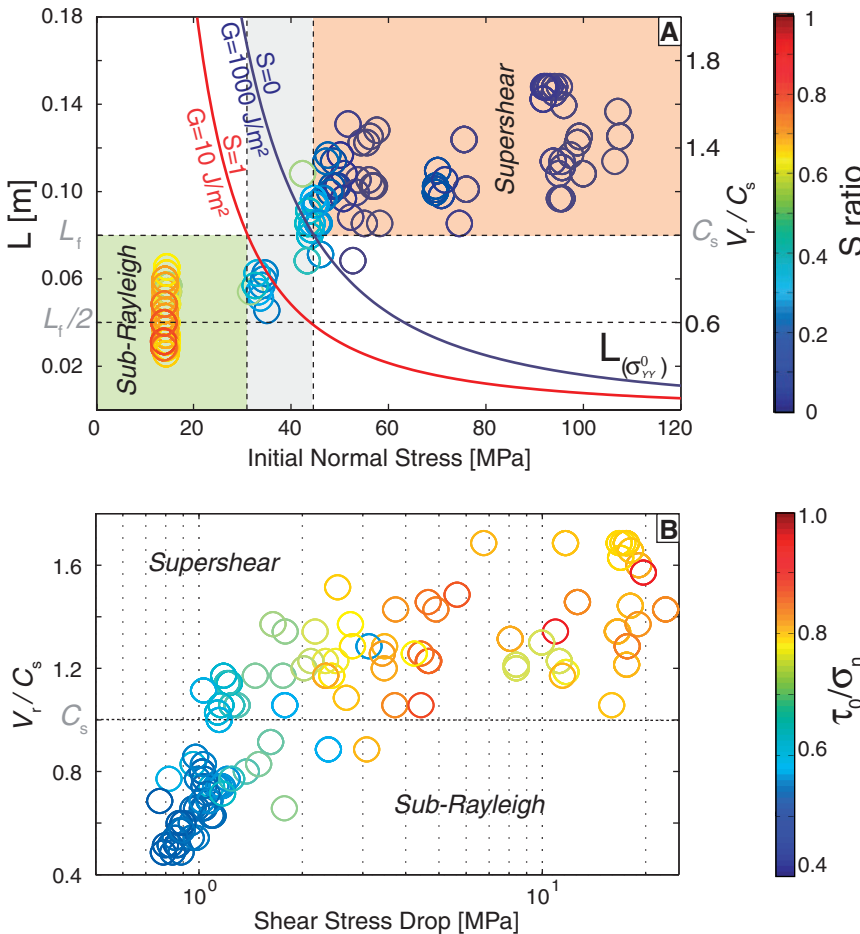


Fig. 4. The transition to supershear ruptures. (A) Correlation between normal stress and rupture velocity. Color-coding corresponds to the value of S . Red and blue solid lines represent L as a function of normal stress, assuming two combinations of S and G . **(B)** Correlation between rupture velocity and stress drop. Color-coding corresponds to the value of τ_0/σ_n . L_f is the length of the experimental fault and $L(\sigma_{yy}^0)$ is the transition length as a function of the normal stress.

References and Notes

1. R. Madariaga, *Ann. Geophys.* **1**, 17 (1983).
2. R. Burridge, *Geophys. J. R. Astron. Soc.* **35**, 439 (1973).
3. R. J. Archuleta, *J. Geophys. Res.* **89**, 4559 (1984).
4. M. Bouchon *et al.*, *Geophys. Res. Lett.* **28**, 2723 (2001).
5. M. Bouchon, M. Vallée, *Science* **301**, 824 (2003).
6. W. L. Ellsworth *et al.*, *Earthq. Spectra* **20**, 597 (2004).
7. P. Liu, S. Custodio, R. J. Archuleta, *Bull. Seismol. Soc. Am.* **96**, 5143 (2006).
8. D. Wang, J. Mori, T. Uchide, *Geophys. Res. Lett.* **39**, L21307 (2012).
9. D. J. Andrews, *J. Geophys. Res.* **81**, 5679 (1976).
10. A. Bizzarri, E. M. Dunham, P. Spudich, *J. Geophys. Res.* **115**, B08301 (2010).
11. F. T. Wu, K. C. Thomson, H. Kuenzler, *Bull. Seismol. Soc. Am.* **62**, 1621 (1972).
12. K. Xia, A. J. Rosakis, H. Kanamori, *Science* **303**, 1859 (2004).
13. S. Nielsen, J. Taddeucci, S. Vinciguerra, *Geophys. J. Int.* **180**, 697 (2010).
14. O. Ben-David, G. Cohen, J. Fineberg, *Science* **330**, 211 (2010).

15. A. Schubnel, S. Nielsen, J. Taddeucci, S. Vinciguerra, S. Rao, *Earth Planet. Sci. Lett.* **308**, 424 (2011).
16. W. F. Brace, J. D. Byerlee, *Science* **153**, 990 (1966).
17. T. L. Johnson, C. H. Scholz, *J. Geophys. Res.* **81**, 881 (1976).
18. P. G. Okubo, J. H. Dieterich, *J. Geophys. Res.* **89**, 5817 (1984).
19. M. Ohnaka, L.-f. Shen, *J. Geophys. Res.* **104**, 817 (1999).
20. M. Mello, H. S. Bhat, A. J. Rosakis, H. Kanamori, *Tectonophysics* **493**, 297 (2010).
21. E. M. Dunham, R. J. Archuleta, *Geophys. Res. Lett.* **32**, L03302 (2005).
22. T.-F. Wong, *J. Geophys. Res.* **87**, 990 (1982).
23. D. P. Robinson, C. Brough, S. Das, *J. Geophys. Res.* **111**, B08303 (2006).
24. T. Candela, F. Renard, *J. Struct. Geol.* **45**, 87 (2012).
25. R. H. Sibson, *Nature* **316**, 248 (1985).
26. J. R. Rice, *J. Geophys. Res.* **111**, B05311 (2006).
27. G. Di Toro, T. Hirose, S. Nielsen, G. Pennacchioni, T. Shimamoto, *Science* **311**, 647 (2006).
28. N. Brantut, A. Schubnel, J.-N. Rouzaud, F. Brunet, T. Shimamoto, *J. Geophys. Res.* **113**, B10401 (2008).
29. M.-L. Doan, G. Gary, *Nat. Geosci.* **2**, 709 (2009).

Acknowledgments: We thank Y. Piquier for technical support and two reviewers and the associate editor for their constructive remarks, which helped to enhance this paper.

F.X.P., A.S., and S.N. acknowledge support from the French and Italian Ministry of Foreign Affairs program GALILEO, project no. 26019WJ. This work was supported by the Institut National des Sciences de l'Univers. Data are available in the supplementary materials.

Supplementary Materials

www.sciencemag.org/cgi/content/full/340/6137/1208/DC1

Materials and Methods

Figs. S1 to S4

Table S1

References

25 January 2013; accepted 15 April 2013

10.1126/science.1235637

Stepwise Evolution of Essential Centromere Function in a *Drosophila* Neogene

Benjamin D. Ross,^{1,2} Leah Rosin,^{3*} Andreas W. Thoma,^{4*} Mary Alice Hiatt,^{2,5*} Danielle Vermaak,^{2*†} Aida Flor A. de la Cruz,^{2,6} Axel Imhof,⁴ Barbara G. Mellone,³ Harmit S. Malik^{2,6‡}

Evolutionarily young genes that serve essential functions represent a paradox; they must perform a function that either was not required until after their birth or was redundant with another gene. How young genes rapidly acquire essential function is largely unknown. We traced the evolutionary steps by which the *Drosophila* gene *Umbrea* acquired an essential role in chromosome segregation in *D. melanogaster* since the gene's origin less than 15 million years ago. *Umbrea* neofunctionalization occurred via loss of an ancestral heterochromatin-localizing domain, followed by alterations that rewired its protein interaction network and led to species-specific centromere localization. Our evolutionary cell biology approach provides temporal and mechanistic detail about how young genes gain essential function. Such innovations may constantly alter the repertoire of centromeric proteins in eukaryotes.

Young essential genes (1) challenge longstanding dogmas about the relationship between essentiality and conservation (2). Partitioning of essential, ancestral functions (subfunctionalization) between (old) parental and (young) daughter genes (3, 4) explains one route by which young genes become essential. More difficult to understand is how new genes become essential via the emergence of novel function (neofunctionalization) (5). This could result from partial duplication of ancestral genes, novel gene fusions, or rapid amino acid changes (6). The contribution of each of these processes to the acquisition of essential function is unknown, as are the underlying molecular changes.

¹Molecular and Cellular Biology Program, University of Washington, Seattle, WA 98195, USA. ²Basic Sciences Division, Fred Hutchinson Cancer Research Center, Seattle, WA 98109, USA. ³Department of Molecular and Cell Biology, University of Connecticut, Storrs, CT 06269, USA. ⁴Munich Centre of Integrated Protein Science and Adolf-Butenandt Institute, Ludwig Maximilians University of Munich, 08336 Munich, Germany. ⁵Law Firm of Fitzpatrick, Cella, Harper & Scinto, New York, NY 10104, USA. ⁶Howard Hughes Medical Institute, Fred Hutchinson Cancer Research Center, Seattle, WA 98109, USA.

*These authors contributed equally to this work.

†Present address: Science-wise Consulting, Seattle, WA 98109, USA.

‡Corresponding author. E-mail: hsmalik@fhcrc.org

To gain insight into the birth and evolution of essential function, we focused on one newly evolved gene in *Drosophila*. *Umbrea* (also known as *HP6* and *CG15636*) arose via duplication of the intronless *Heterochromatin Protein 1B* (*HP1B*) gene into an intron of the *dumpy* gene (Fig. 1A) (7). *HP1B* is a chromosomal protein that predominantly localizes to heterochromatin in *D. melanogaster* cells and regulates gene expression (8). *HP1B* is dispensable for viability (8), yet RNA interference (RNAi) knockdown phenotypes show *Umbrea* to be essential in *D. melanogaster* (1, 9). The 100% late larval-pupal lethality upon *Umbrea* knockdown could be rescued by an *Umbrea*-green fluorescent protein (GFP) fusion (fig. S1) further confirmed that *Umbrea* is essential in *D. melanogaster*.

We traced *Umbrea*'s evolutionary path after duplication from *HP1B* to understand when and how essential function was gained by comparing the localization of *HP1B* and *Umbrea* proteins in *D. melanogaster* Kc cells. GFP-tagged *HP1B* proteins from both *D. melanogaster* and *D. ananassae* [whose divergence predates the birth of *Umbrea* (7)] localized to pericentric heterochromatin and euchromatin (Fig. 1B and fig. S2). In contrast, *Umbrea*-GFP predominantly localized to interphase centromeres, but not telomeres (Fig. 1C

and fig. S3, A and B). Specific antibodies raised against *Umbrea* (fig. S4A) confirmed its centromere localization in developing spermatocytes and larval imaginal discs (Fig. 1, D and E, and fig. S4, B and C).

On the basis of its essentiality and centromere localization, we hypothesized that *Umbrea* was required for chromosome segregation. Upon depletion of *Umbrea* by RNAi knockdown (fig. S5A), relative to control cells, *D. melanogaster* S2 cells displayed increased mitotic errors, including delayed chromosome alignment, early anaphase onset, lagging anaphase chromosomes, and multipolar configurations ($P < 0.05$) (Fig. 1, F and G, fig. S5B, and movies S1 to S3). These data suggest that *Umbrea* promotes proper chromosome segregation, but is not required for the localization of the centromeric histone Cid (Fig. 1F).

To date the origin of *Umbrea* and subsequent changes, we sequenced the *Umbrea* locus from 32 *Drosophila* species (fig. S6A). Whereas *HP1B* was preserved (7), we found *Umbrea* in only 20 of 32 species, dating its monophyletic origin to 12 to 15 million years ago (Fig. 2A and fig. S6B). Using maximum likelihood methods, we observed evidence of both episodic and recurrent positive selection acting on *Umbrea* (fig. S7, A to D). These findings, together with the altered localization, lead us to conclude that neofunctionalization, not subfunctionalization, drove the divergence of *Umbrea* (10). Although *Umbrea* is essential in *D. melanogaster*, it was lost at least three independent times—in *D. fujyamai*, *D. eugracilis*, and in the *suzukii* clade (Fig. 2A)—which suggests that *Umbrea* was not essential at or immediately after its birth.

Four lineages retained full-length *Umbrea* genes, two of which encode an intact chromodomain (CD) and ancestral residues essential for binding histone H3 trimethyl Lys⁹ (H3K9me) (fig. S8) (11). However, most extant *Umbrea* genes have lost their CDs, and encode only the chromoshadow domain (CSD), which mediates protein-protein interactions (12) (Fig. 2A). We first tested how CD loss affected *HP1B* function. We found that an *HP1B*-GFP fusion lacking the CD lost heterochromatin localization (Fig. 2B), consistent with the requirement of *HP1B* CD for H3K9me binding (13). Furthermore, fusion of the *HP1B* CD and hinge to *Umbrea*-GFP reverted localization from centromeres to heterochromatin (Fig. 2C), which suggests that loss of the ancestral CD